

# Single-Spin Nitrogen-Vacancy Magnetometer with Enhanced Static Field Sensitivity

Vinaya K. Kavatamane,<sup>\*,†,§</sup> Dewen Duan,<sup>†,||</sup> Hadi Zadeh-Haghighi,<sup>‡</sup> Manh-Huong Phan,<sup>¶</sup> and Gopalakrishnan Balasubramanian<sup>\*,†,⊥</sup>

<sup>†</sup>*Max Planck Research Group - Nanoscale Spin Imaging, Max Planck Institute for Biophysical Chemistry, Am Fassberg 11, 37077, Göttingen, Germany*

<sup>‡</sup>*QNeura, Calgary, Alberta T2L 0Y2, Canada*

<sup>¶</sup>*Center for Materials Innovation and Technology, VinUniversity, Hanoi 100000, Vietnam*

<sup>§</sup>*Current address: Institute for Quantum Science and Technology, University of Calgary, Calgary, Alberta T2N 1N4, Canada*

<sup>||</sup>*Current address: School of Physics and Electronic Engineering, Sichuan University of Science and Engineering, Yibin 644005, China*

<sup>⊥</sup>*Current address: XeedQ GmbH, Augustusplatz 1-4, 04109 Leipzig, Germany*

E-mail: vinayakumar.kavatama@ucalgary.ca; gopi@xeedq.com

## Abstract

Precision sensing and imaging of weak static magnetic fields are crucial for a variety of emerging nanoscale applications. While nitrogen-vacancy (NV) centers in diamond provide exceptional AC magnetic field sensitivity with nanoscale spatial resolution, their sensitivity to static (DC) magnetic fields is fundamentally limited by the short dephasing time ( $T_2^*$ ) due to spin-spin interactions. In this work, we present a novel hybrid sensing approach that integrates a soft ferromagnetic microwire with a single near-surface NV center to amplify its response to

external static magnetic fields. This hybrid configuration achieves a DC magnetic field sensitivity of  $63 \text{ nT}/\sqrt{\text{Hz}}$  for a single NV center—about 500 times greater than conventional inhomogeneous broadening- or  $T_2^*$ -limited magnetometry, with potential for further enhancement. The compact and highly sensitive nature of this sensor opens new opportunities for quantum sensing applications involving the detection of static or slowly varying magnetic fields across diverse scientific and technological domains.

The ability to detect weak magnetic fields with high sensitivity and spatial resolution forms an indispensable task across many areas of modern science and has the potential to enable transformative applications in fields ranging from fundamental physics<sup>1-3</sup> and materials science<sup>4</sup> to biological research.<sup>5</sup> Over the past few decades, a variety of magnetic field sensors have been developed, some of which achieve remarkable levels of sensitivity.<sup>6-8</sup> Notable examples include superconducting quantum interference devices (SQUIDs)<sup>9</sup> and optically pumped magnetometers (OPMs),<sup>6,10,11</sup> both of which can detect magnetic fields with sensitivities surpassing a femto-Tesla. However, these technologies typically suffer from significant limitations, such as the need for cryogenic operation, high power consumption, and limited spatial resolution.

As an alternative, individual nitrogen-vacancy (NV) centers in diamond have emerged as highly promising magnetic field sensors, offering nanoscale spatial resolution and operation under ambient conditions.<sup>12-14</sup> These solid-state quantum sensors exploit the long coherence times ( $T_2$ ) of NV center spins for the detection of oscillating (AC) magnetic fields,<sup>15,16</sup> achieving sensitivities ( $\eta_{ac}$ ) in the nano-Tesla range.<sup>16,17</sup> However, the sensitivity of NV centers to static (DC) magnetic fields is significantly lower—typically around  $10 \mu\text{T}$ —and is fundamentally limited by the shorter dephasing time ( $T_2^*$ , where  $T_2^* < T_2$ ), such that  $\eta_{dc} \propto 1/\sqrt{T_2^*}$ .<sup>18</sup> This challenge is particularly pronounced for shallow NV centers embedded in diamond crystals with natural  $^{13}\text{C}$  abundance, which are commonly used for nanoscale sensing applications.<sup>19,20</sup> In these cases, the proximity to surface-related noise sources further degrades  $T_2^*$ , thereby limiting their full potential for static magnetic field detection.

In this work, we present a novel approach that leverages the significantly longer  $T_2$  time of

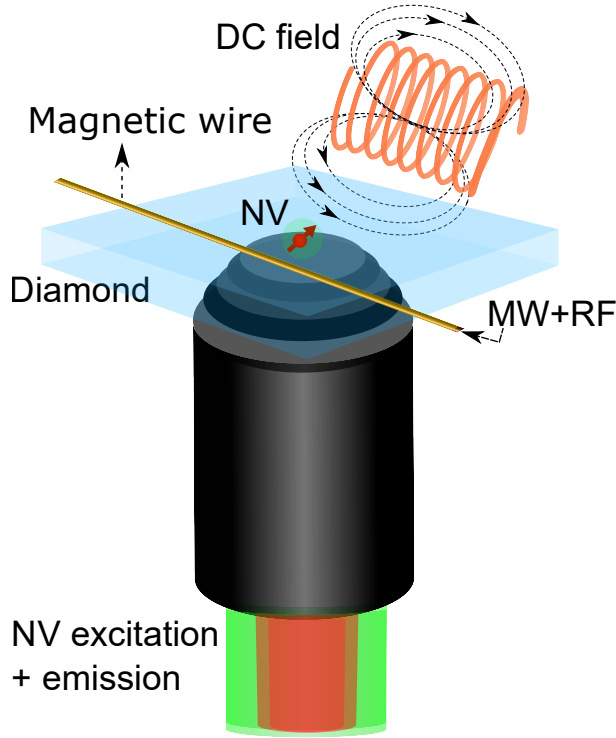


Figure 1: (a) A simplified schematic of the GMI–NV-based hybrid sensor setup is shown. A soft ferromagnetic (GMI) wire is positioned on top of a diamond wafer containing individual shallow NV centers (indicated by a red sphere with an arrow). A microscope objective, aligned through the wafer, is used to focus a green excitation laser and collect the resulting NV fluorescence. Microwave pulses, used to manipulate the NV spin states, and a radio-frequency waveform, used to activate the GMI effect, are applied simultaneously through the GMI wire. A nearby coil generates the DC test magnetic field to be detected.

shallow NV centers to achieve a  $\eta_{dc}$  of  $63 \text{ nT}/\sqrt{\text{Hz}}$ . This represents a substantial improvement over the conventional Ramsey method, which typically yields  $\eta_{dc}$  on the order of tens of  $\mu\text{T}$ . Our method enhances  $\eta_{dc}$  by exploiting near-field magnetic interactions between the NV center and a magnetic microwire exhibiting ‘giant magneto-impedance’ (GMI) response. Notably, the demonstrated sensitivity of  $62 \text{ nT}/\sqrt{\text{Hz}}$  for a shallow NV center exceeds that of the best-reported single NV sensitivities in bulk diamond (approximately  $300 \text{ nT}^{21}$ ) despite the latter’s superior isolation from surface noise. This improvement highlights the potential of our approach for highly sensitive external magnetic field sensing with shallow NV centers.

Magneto-impedance response of certain soft ferromagnetic materials offers a highly sensitive mechanism for magnetic field detection.<sup>22</sup> In that context, GMI effect in ferromagnetic alloys is a classical phenomenon which occurs when a small change in the DC magnetic field ( $H_{dc}$ ) in their

vicinity causes a large changes in their AC complex impedance ( $Z$ ).<sup>23–26</sup> The GMI effect has its origin in the *skin effect* wherein the penetration depth of AC current depends on its frequency ( $f_{ac}$ ) and the relative permeability ( $\mu_r$ ) of the material. See section-iii of *Supporting Information (SI)*, for more details. In the so-called intermediate frequency range—from approximately  $f_{ac} \approx 100$  kHz to  $\approx 1$  GHz—materials exhibit electrical impedance that is highly sensitive to external DC magnetic fields.<sup>27</sup> Within this range, even a small DC field on the order of a fraction of a milli-Tesla can produce a substantial change in impedance. The relative change is quantified by the GMI ratio:

$$\frac{\Delta Z}{Z} = \frac{Z(H_{dc}) - Z(H'_{dc})}{Z(H'_{dc})} \times 100\% \quad (1)$$

where  $\Delta Z$  is the change in impedance, and  $Z(H_{dc})$  is the impedance at a given external DC magnetic field  $H_{dc}$ , and  $Z(H'_{dc})$  is the impedance at a maximum field  $H'_{dc}$ , typically chosen to be large enough to saturate the magneto-impedance response. This GMI ratio can reach values as high as 500%, highlighting the material’s strong magneto-impedance response even under weak magnetic fields.<sup>22</sup> A typical response of the GMI ratio ( $\frac{\Delta Z}{Z}$ ) as a function of external DC magnetic field amplitude is shown in Fig. S2(a) of the *SI*. This characteristic behavior is well established in the GMI research community. The pronounced field-dependent impedance response has enabled the development of highly sensitive magnetic field sensors capable of detecting fields down to pico-Tesla scale under ambient conditions.<sup>26,28,29</sup> However, the reliance on traditional induction-based readout schemes results in relatively bulky sensor designs, thereby limiting spatial resolution to the millimeter scale.<sup>26,29–31</sup> This size constraint presents a major challenge for the continued miniaturization of GMI-based sensor platforms.

On the other hand, nitrogen-vacancy (NV) centers in diamond are well established as highly sensitive quantum sensors for magnetic fields.<sup>19,32</sup> Due to their atomic-scale size, these sensors can be positioned within nanometers of a target, enabling spatial resolution at the nanometer scale.<sup>12,15,33</sup>

In this work, we demonstrate a hybrid magnetic field sensing system that integrates a GMI wire of the composition  $\text{Co}_{69.25}\text{Fe}_{4.25}\text{Si}_{13}\text{B}_{12.5}\text{Nb}_1$ , a classical sensor, with a quantum NV center

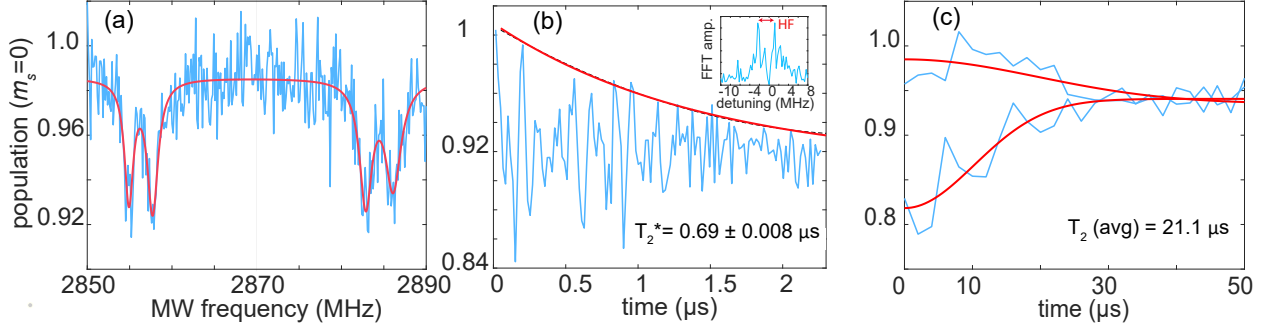


Figure 2: Electron spin resonance measurements of an individual shallow NV center in the presence of stray magnetic field from the magnetic wire. (a) ODMR spectrum. Due to the presence of stray magnetic field from the wire ( $\sim 0.5$  mT), NV center's otherwise degenerate  $m_s = \pm 1$  spin sub levels are split from the zero field line  $D = 2870$  MHz. Red solid line is a Lorentzian fit to the data. The two dips at a separation of  $\sim 3$  MHz on either side of  $D$  indicate the presence unpolarised  $^{15}\text{N}$  nuclear spin of the NV center. (b) Ramsey interference signal exhibiting a decay with a characteristic timescale of  $T_2^* = 0.69 \mu\text{s}$ . The red line represents an exponential fit to the envelope of the oscillations. Inset: Fast Fourier transform (FFT) of the Ramsey signal as a function of detuning frequency, showing a hyperfine splitting (3 MHz) corresponding to  $^{15}\text{N}$  nuclear spin, as identified in (a). (c) Hahn-echo measurement. The top and bottom blue traces correspond to echo signals with the phase of the initial  $\frac{\pi}{2}$  pulse shifted by  $180^\circ$  between the two traces. The red lines are fits to extract coherence decay. The average coherence time  $T_2$  from both fits is  $21 \mu\text{s}$ .

sensor, achieving both high sensitivity and nanoscale spatial resolution. To realize this, a GMI microwire was placed on top of a diamond chip containing shallow-implanted NV centers located a few nanometers beneath the surface<sup>34</sup> (Fig.1(a)). We characterized the sensitivity of this hybrid NV-GMI sensor to external DC magnetic fields ( $B_{\text{dc}}$ ). A high numerical aperture ( $\text{NA} = 1.35$ ) oil-immersion microscope objective was used to image individual NV centers, and confocal fluorescence images of the diamond sample were obtained. See section i-ii of *SI* for details of the experimental setup and sample preparation. As illustrated in Fig.1(a), microwave (MW) pulses for NV spin manipulation and radio frequency (RF) signals to induce the GMI effect were simultaneously delivered to the wire via two separate channels of an arbitrary waveform generator. The GMI wire also serves as a microwave antenna, eliminating the need for a separate dedicated antenna (such as a copper wire) and thereby simplifying the experimental design.

A nearby coil, driven by a variable DC current source, generates the external  $B_{\text{dc}}$  to be measured. In this configuration, the GMI wire responds to changes in the external magnetic field, and the response is read out with high sensitivity by a single NV quantum sensor.

Since the wire is magnetic, there always exists a stray field in the vicinity of the wire<sup>35</sup> (typical coercive field is  $\sim 2$  Oe). As a result, a NV center situated near the wire typically experiences a static field of a few hundred  $\mu$ -Tesla originating from the magnetic domains of the wire. This static field acts as a small bias field which will split the degenerate  $m_s = \pm 1$  spin sublevels of the NV spin in its ground state. The presence of small stray static field eliminates the need for applying an external bias magnetic field for the NV center, thereby further simplifying the sensor setup.

Optically detected magnetic resonance (ODMR) is a straight forward way to measure the magnitude of the stray field at each NV center.<sup>36</sup> By individually performing ODMR measurements on multiple NV centers located at various positions around the wire, a wide-field magnetic image of the wire can be reconstructed (see section-v in *SI*). It is important to note that the static magnetic field generated by the wire exhibits a complex spatial profile; therefore, the direction and magnitude of the field experienced by each NV center vary with position. For the magnetometry experiments, we selected only those NV centers that exhibited symmetric and sufficiently large splitting in their ODMR spectra relative to the zero-field splitting parameter. Figure 2(a) shows a representative ODMR spectrum for one such NV center. Unless otherwise stated, all data and analyses presented in this work correspond to this specific NV center.

For all subsequent measurements, including magnetometry, we employ the NV spin transition between the  $m_s = 0$  and  $m_s = -1$  manifold. We obtained Rabi frequencies ( $\Omega_R$ ) in the range of 10 MHz. For measuring the spin dephasing timescale ( $T_2^*$ ), a standard Ramsey measurement protocol was used, employing the pulse sequence  $\frac{\pi}{2} - \tau - \frac{\pi}{2}$ , inserted between two laser pulses—one for spin initialization and another for readout—where  $\tau$  is the variable free precession time. This measurement yielded a  $T_2^*$  coherence time of approximately  $0.7 \mu\text{s}$  (Fig. 2(b)), which is typical for shallow NV centers prepared with standard diamond surface treatments (see section-ii of *SI*).

The Fourier transform of the Ramsey signal reveals hyperfine (HF) splitting (inset of Fig. 2(b)), corresponding to the implanted  $^{15}\text{N}$  nuclear spin intrinsic to the NV center. The extracted full width at half maximum (FWHM) linewidth ( $\delta\nu$ ) of one HF transition is  $0.9 \pm 0.12$  MHz. Once  $\delta\nu$  is known, the minimum resolvable external magnetic field  $\delta B$  can be estimated using the energy

equation  $h\delta\nu = g\mu_B\delta B$ , where  $h$  is Planck's constant,  $g$  is the electron g-factor ( $g = 2.0$ ), and  $\mu_B$  is the Bohr magneton. Based on this equation, our measured linewidth corresponds to a photon shot-noise-limited magnetic field sensitivity of approximately  $32 \mu\text{T}$ .

Application of a Hahn-echo sequence  $\frac{\pi}{2} - \tau - \pi - \tau - \frac{\pi}{2}$  can effectively extend the coherence time from  $T_2^*$  to a long-lived  $T_2$  timescale.<sup>15,16</sup> In figure 2(c) the data for Hahn-echo sequence was fitted to a stretched exponential function,  $Ae^{-\left(\frac{\tau}{T_2}\right)^p}$ , where  $A$  is the signal amplitude and  $p = 2$ , to extract the time constant  $T_2$  value. We obtain a  $T_2$  value of  $21 \mu\text{s}$  which effectively enhanced the coherence time by a factor of 30 compared to the  $T_2^*$  measured above.

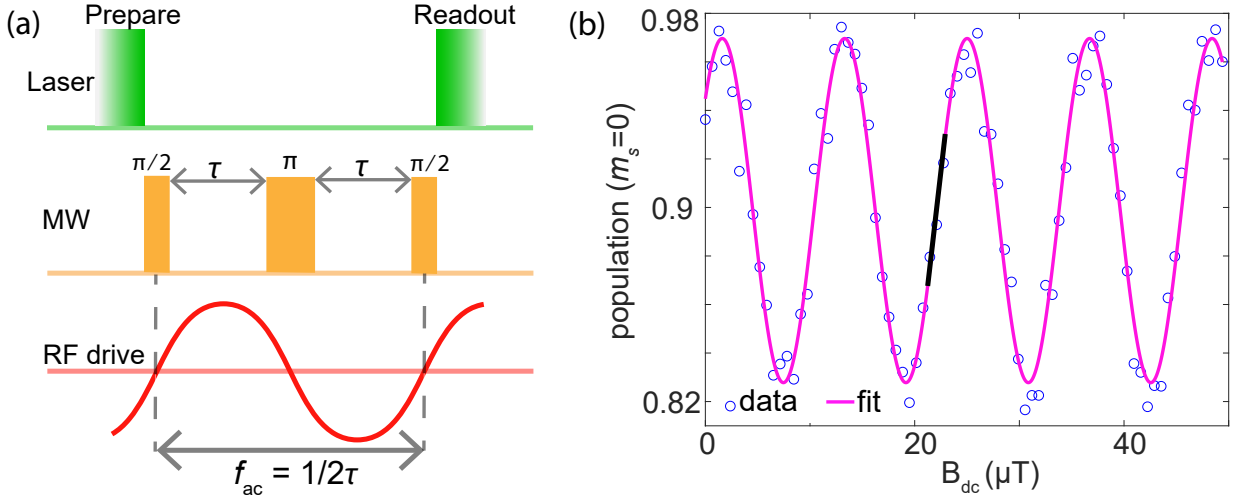


Figure 3: Demonstration of DC magnetic field sensitivity of the NV-GMI hybrid sensor. (a) Schematic representation of the DC magnetometry. A Hahn-echo sequence with a fixed  $\tau$  was applied to the NV. The GMI wire was simultaneously driven by a RF signal whose frequency was matched to the echo period ( $f_{ac} = 1/2\tau$ ) (b) Oscillatory response of the magnetometer signal as a function of the amplitude of the external DC magnetic field. The  $f_{ac}$  was set to 100 kHz. The data was fitted to a sinusoidal function. The sensitivity of the sensor is calculated from the maximum slope (black straight line) of the response.

To detect weak external magnetic fields, we employ a Hahn-echo-based magnetometry technique integrated with a hybrid NV-GMI sensor. In conventional Hahn-echo sequences, the accumulated quantum phase of the NV center over the free precession periods cancels out, rendering the method inherently insensitive to static magnetic fields.<sup>16,17</sup> As a result, the NV spin ideally returns to its original state ( $m_s = 0$ ) at the end of the sequence.

In our approach, however, we circumvent this insensitivity by leveraging the field-dependent response of the GMI wire.<sup>35</sup> The GMI wire acts as a transducer, converting variations in external

static fields into changes in its impedance, which in turn modulates the local magnetic environment sensed by the NV center during the echo sequence.

The experimental protocol involved a standard Hahn-echo sequence with a fixed precession interval  $2\tau$  (see Fig.3(a)), applied to the NV center. Concurrently, a time-varying RF drive voltage,  $v(t') = v_{ac} \sin(2\pi f_{ac} t' + \phi')$ , was applied to the GMI wire, where  $v_{ac}$ ,  $f_{ac}$ , and  $\phi'$  denote the amplitude, frequency, and phase, respectively. The RF frequency was chosen to satisfy  $f_{ac} = 1/2\tau$ , ensuring synchronization with the echo sequence. Importantly, the value of  $f_{ac}$  was selected such that it falls within the optimal operating regime of the GMI effect—i.e., where the  $Z$  of the wire exhibits strong sensitivity to external DC magnetic fields.<sup>23–25</sup> The phase  $\phi'$  was fixed at zero for all measurements.

Under this RF excitation, the GMI wire exhibits enhanced sensitivity to nearby static magnetic fields. Changes in the local DC magnetic field alter the wire's  $Z$ , thereby modulating its magnetic behavior. Since the NV center couples magnetically to the GMI wire, these  $Z$ -induced changes influence the NV's spin evolution during the echo sequence, ultimately altering its fluorescence signal.

To probe this interaction, we gradually varied the amplitude of an externally applied static magnetic field  $B_{dc}$  and observed periodic oscillations in NV fluorescence intensity (Fig.3(b)). This fluorescence modulation encodes information about the field strength and enables quantitative field sensitivity analysis. The minimum detectable magnetic field  $B_{min}$  was extracted using:

$$B_{min} = \frac{\sigma_s}{\left(\frac{dS}{dB_{dc}}\right)}, \quad (2)$$

where  $\sigma_s$  is the standard deviation of the fluorescence signal ( $S$ ), and  $\frac{dS}{dB_{dc}}$  is the maximum slope of the signal response curve shown in Fig.3(b). For an RF driving frequency of 100 kHz (corresponding to  $2\tau = 10\mu s$ ), we achieved a static field sensitivity of  $\eta_{dc} = B_{min}\sqrt{t} = 62.5\text{ nT}/\sqrt{\text{Hz}}$ , where  $t$  is the total measurement time (see section-viii in *SI* for error analysis). This sensitivity represents a 500X improvement over the estimated Ramsey-based DC field sensitivity ( $32\mu\text{T}$ )

mentioned earlier for the same NV center, demonstrating the enhanced performance of the hybrid NV-GMI magnetometer in detecting weak static magnetic fields. This enhanced  $\eta_{dc}$  of our sensor arises from two key factors. First, the GMI wire intrinsically exhibits a high sensitivity to external static magnetic fields far exceeding the Ramsey-based NV sensitivity. Second, the use of an echo sequence, rather than a Ramsey sequence, significantly extends the NV coherence time by mitigating inhomogeneous dephasing. This extension beyond the  $T_2^*$ -limit allows for longer interrogation times and thus improves the overall  $\eta_{dc}$ .

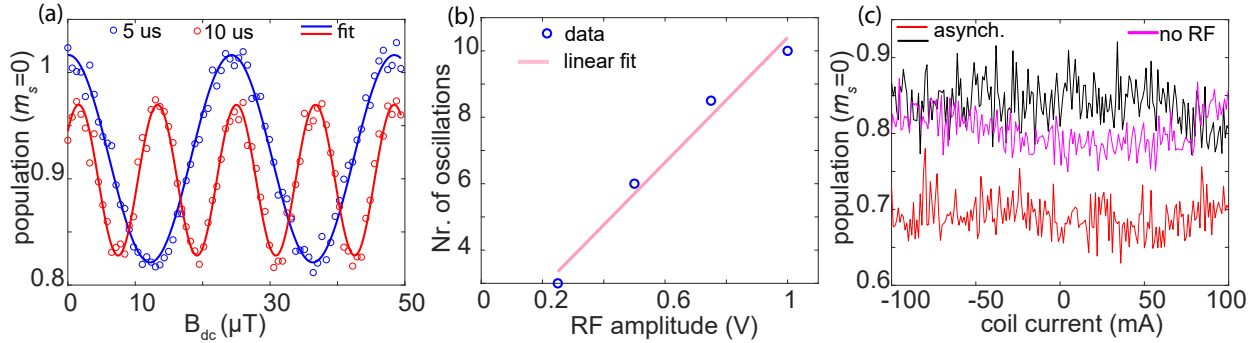


Figure 4: (a) NV-GMI hybrid magnetometer signal for different RF drive frequency (equivalently  $1/2\tau$ ). Decreasing the  $\tau$  gives higher signal contrast but at the expense of halved phase acquired by the NV and hence the reduced  $\eta_{dc}$ . (b) Number of oscillations of the magnetometer signal vs. amplitude of the RF drive voltage across the GMI wire. (c) Magnetometer signal as a function of external  $B_{dc}$  amplitude for three different conditions: no RF drive applied to the GMI wire (magenta), RF drive with asynchronous frequency (black), and RF drive with asynchronous phase (red). For clarity, the traces are vertically offset. Note that  $B_{dc}$  values are represented in terms of the raw current applied to the field-generating coil.

Note that we chose a nominal value of  $2\tau$  ( $1/f_{ac} = 10 \mu\text{s}$ ) where the NV center's coherence is sufficient to provide a good signal-to-noise ratio in the spin contrast and which also allows for the GMI effects to occur. If we increase the  $\tau$ , number of oscillations in the magnetometer signal correspondingly increases at the cost of reduced NV spin contrast (Fig.4(a)) due to loss of coherence. Since the number of oscillations in the magnetometer signal directly contributes to improved sensitivity, maximizing these oscillations becomes desirable. The number of oscillations scales linearly (Fig.4(b)) with the RF drive amplitude. Therefore, throughout all measurements, the sensor was operated at the maximum allowable RF amplitude to optimize sensitivity.

To confirm that the observed oscillations in the magnetometer signal originate from the NV

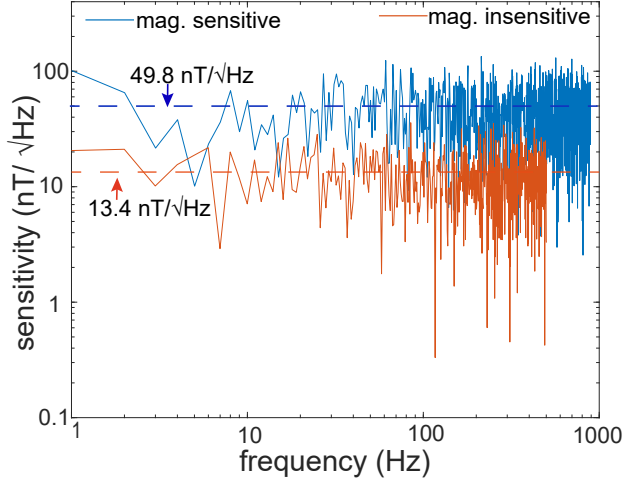


Figure 5: Noise spectral density of the hybrid NV-GMI magnetometer. The sensor was operated at maximum sensitivity by applying the RF drive signal at optimal frequency and maximum amplitude, with the Hahn-echo sequence synchronized to the drive. The magnetically sensitive trace was recorded under the application of a small static test field.

center’s magnetic interaction with the GMI wire, and not from experimental artifacts, we performed control experiments with varying conditions. First, we set the RF drive amplitude to zero and applied a fixed- $\tau$  echo sequence (as shown in Fig.3(a)) to the NV center while varying the external  $B_{dc}$  amplitude in discrete steps. At each step, the corresponding NV fluorescence was recorded. In the absence of RF excitation, the fluorescence signal remained flat, showing almost no oscillatory behavior (Fig.4(c)). In contrast, when the RF drive was turned on, oscillations were revived, and their number increased with increasing RF drive strength (Fig.4(b)). Furthermore, no oscillations were observed when the RF signal was applied asynchronously with respect to the NV echo sequence—either in frequency ( $f_{ac} \neq 1/2\tau$ ) or in phase ( $\phi' \neq 0$ ) as seen in Fig.4(c). This indicates a coherent interaction exists between the GMI element and NV, and a precise synchronization of the RF drive with the NV echo sequence is needed. These results confirm that the oscillations arise from the near-field magnetic coupling between the NV center and the GMI wire, mediated by the RF-induced modulation of the wire’s  $Z$ .

Figure5 presents the noise spectral density of the hybrid NV-GMI magnetometer. For the magnetically sensitive configuration, the sensitivity exhibits a mean noise floor of  $\approx 49.8 \text{ nT}/\sqrt{\text{Hz}}$ . These data were acquired using the magnetometry protocol described in Fig.3(a), with a constant

but small value of external  $B_{dc}$  applied via the field-generating coil (see section-viii in *SI*). To our knowledge, the best reported DC field sensitivities for GMI-based sensors lie in the range of 1–100 pT/ $\sqrt{\text{Hz}}$ .<sup>37</sup> Therefore, there is still a room for nearly 1000X improvement in sensitivity for the hybrid sensing modality presented in this work. Nevertheless, this modality offers a highly sensitive platform for DC magnetometry with nanoscale spatial resolution—something not achievable with conventional GMI sensors alone. For comparison, Fig.5 also shows the background noise spectrum with a mean noise floor value of  $\approx 13.4$  nT/ $\sqrt{\text{Hz}}$ , recorded with all microwave, RF, and laser sources turned off. This background originates primarily from ambient light leakage into the photon detector and exhibits a slightly lower noise floor than the magnetically sensitive case.

The NV-GMI-based Hahn-echo magnetometry demonstrated in this work serves as a proof-of-concept, and there is considerable scope for further improving the  $\eta_{dc}$  of this hybrid sensing platform. One promising avenue is to extend the NV center’s coherence time  $T_2$  beyond what is achievable with the Hahn-echo sequence by employing dynamical decoupling protocols, which would directly enhance sensitivity. Additionally, implementing double-quantum magnetometry techniques<sup>38</sup> could, in principle, offer up to a 2-fold improvement in  $\eta_{dc}$ . A more substantial enhancement, potentially an order of magnitude, can be gained by improving the NV photon collection efficiency. This can be achieved through nanophotonic engineering, such as the use of diamond nanopillar waveguides<sup>39</sup> or circular diamond gratings.<sup>40</sup> Further gains are possible by adopting spin-to-charge conversion techniques<sup>41</sup> or by absorption of NV singlet states,<sup>42</sup> which enable higher-fidelity spin readout than that is achieved with fluorescence detection. With these efforts, the projected sensitivity of the hybrid NV-GMI sensor could reach the level of a few nT/ $\sqrt{\text{Hz}}$ , approaching the AC field sensitivity of single NV centers<sup>16</sup>—but notably, without the need for specially engineered or high-purity diamond samples. Instead of single NV centers, if ensemble NV centers are used then the  $\eta_{dc}$  of the resulting hybrid sensor would scale as  $1/\sqrt{N}$  ( $N$  is the number of NVs in the sensing volume), at the expense of spatial resolution. It is worth noting that the  $\eta_{dc}$  of the hybrid-sensor can further be tuned and optimized by varying the dimension and the GMI characteristics of the wire itself. Overall, given the state-of-the-art ensemble NV sensors offer  $\eta_{dc}$

below a pico-Tesla,<sup>43</sup> a further improvement in  $\eta_{\text{dc}}$  of a hybrid NV-GMI sensor could take it close to spin projection limit, thus being on-par with SQUIDs and OPMs.

A sensitive NV-GMI magnetometer is well-suited for detecting static or slowly varying magnetic fields in the following areas. In biomedical applications, it could enable high-resolution, extracellular detection of neuronal activity;<sup>44</sup> in medical diagnostics, perform magnetoencephalography and magnetocardiography under ambient conditions, which require  $\sim 100 \text{ fT}/\sqrt{\text{Hz}}$ <sup>45</sup> and  $\sim 1 \text{ pT}/\sqrt{\text{Hz}}$ ,<sup>46</sup> respectively— thus offering a cryogen-free alternative to SQUID-based systems while substantially reducing the sensor-to-specimen stand-off distance. Furthermore, scaling down from the micrometer-scale GMI wire used in this study to a thin film or a nanowire, and integrating it with a single NV center, could pave the way for highly sensitive detection of magnetically functionalized biomolecules through their binding to the GMI element (see ref.<sup>47</sup>)—potentially enabling single-molecule sensitivity. A compact and highly sensitive nature of the NV-GMI sensor would potentially be advantageous for practical deployment of quantum sensors in applications such as geophysical surveying, mineral exploration, and precision navigation.

In summary, we have presented a hybrid DC magnetic field sensor that leverages the high sensitivity of a magneto-impedance material and the quantum properties of near-surface NV centers in diamond under ambient conditions. This approach achieves field sensitivities over two orders of magnitude greater than conventional  $T_2^*$ -based NV magnetometers. By eliminating the need for a separate microwave antenna and bias field, the sensor significantly simplifies the experimental setup and enables a compact footprint. Combined with its nanoscale spatial resolution, this platform offers a promising route toward advanced, deployable diamond-based quantum sensors for high-resolution detection of slowly varying magnetic fields in a broad range of applications.

## Acknowledgement

The authors (VKK, DD, and GB) thank the funding from the Max-Planck Society, Niedersächsisches Ministerium für Wissenschaft und Kultur. VKK thanks Paul Barclay for the financial support

during the preparation of manuscript and Nicolas Sorensen for discussions.

## References

- (1) Budker, D.; Graham, P. W.; Ledbetter, M.; Rajendran, S.; Sushkov, A. O. Proposal for a Cosmic Axion Spin Precession Experiment (CASPEr). Phys. Rev. X **2014**, 4, 021030.
- (2) DeMille, D.; Doyle, J. M.; Sushkov, A. O. Probing the frontiers of particle physics with tabletop-scale experiments. Science **2017**, 357, 990–994.
- (3) Bass, S. D.; Doser, M. Quantum sensing for particle physics. Nature Reviews Physics **2024**, 6, 329–339.
- (4) Ripka, P. Magnetic sensors and magnetometers; Artech house, 2021.
- (5) Mostufa, S.; Yari, P.; Rezaei, B.; Xu, K.; Wu, K. Flexible magnetic field nanosensors for wearable electronics: A review. ACS Applied Nano Materials **2023**, 6, 13732–13765.
- (6) Shah, V. K.; Wakai, R. T. A compact, high performance atomic magnetometer for biomedical applications. Physics in Medicine & Biology **2013**, 58, 8153.
- (7) Degen, C. L.; Reinhard, F.; Cappellaro, P. Quantum sensing. Rev. Mod. Phys. **2017**, 89, 035002.
- (8) Mitchell, M. W.; Palacios Alvarez, S. Colloquium: Quantum limits to the energy resolution of magnetic field sensors. Reviews of Modern Physics **2020**, 92, 021001.
- (9) Weinstock, H. SQUID Sensors: Fundamentals, Fabrication and Applications, 1st ed.; Springer Netherlands, 1996.
- (10) Kominis, I. K.; Kornack, T. W.; Allred, J. C.; Romalis, M. V. A subfemtotesla multichannel atomic magnetometer. Nature **2003**, 422, 596–599.
- (11) Budker, D.; Romalis, M. Optical magnetometry. Nature Physics **2007**, 3, 227–234.

- (12) Balasubramanian, G.; Chan, I. Y.; Kolesov, R.; Al-Hmoud, M.; Tisler, J.; Shin, C.; Kim, C.; Wojcik, A.; Hemmer, P. R.; Krueger, A.; Hanke, T.; Leitenstorfer, A.; Bratschitsch, R.; Jelezko, F.; Wrachtrup, J. Nanoscale imaging magnetometry with diamond spins under ambient conditions. Nature **2008**, 455, 648–652.
- (13) Degen, C. L. Scanning magnetic field microscope with a diamond single-spin sensor. Applied Physics Letters **2008**, 92, 243111.
- (14) Rovny, J.; Gopalakrishnan, S.; Jayich, A. C. B.; Maletinsky, P.; Demler, E.; de Leon, N. P. Nanoscale diamond quantum sensors for many-body physics. Nature Reviews Physics **2024**, 1–16.
- (15) Taylor, J. M.; Cappellaro, P.; Childress, L.; Jiang, L.; Budker, D.; Hemmer, P. R.; Yacoby, A.; Walsworth, R.; Lukin, M. D. High-sensitivity diamond magnetometer with nanoscale resolution. Nature Physics **2008**, 4, 810 EP –.
- (16) Balasubramanian, G.; Neumann, P.; Twitchen, D.; Markham, M.; Kolesov, R.; Mizuochi, N.; Isoya, J.; Achard, J.; Beck, J.; Tissler, J.; Jacques, V.; Hemmer, P. R.; Jelezko, F.; Wrachtrup, J. Ultralong spin coherence time in isotopically engineered diamond. Nature Materials **2009**, 8, 383–387.
- (17) Maze, J. R.; Stanwix, P. L.; Hodges, J. S.; Hong, S.; Taylor, J. M.; Cappellaro, P.; Jiang, L.; Dutt, M. V. G.; Togan, E.; Zibrov, A. S.; Yacoby, A.; Walsworth, R. L.; Lukin, M. D. Nanoscale magnetic sensing with an individual electronic spin in diamond. Nature **2008**, 455, 644–648.
- (18) Barry, J. F.; Schloss, J. M.; Bauch, E.; Turner, M. J.; Hart, C. A.; Pham, L. M.; Walsworth, R. L. Sensitivity optimization for NV-diamond magnetometry. Rev. Mod. Phys. **2020**, 92, 015004.
- (19) Schirhagl, R.; Chang, K.; Loretz, M.; Degen, C. L. Nitrogen-vacancy centers in diamond:

- nanoscale sensors for physics and biology. Annual review of physical chemistry **2014**, 65, 83–105.
- (20) Casola, F.; Van Der Sar, T.; Yacoby, A. Probing condensed matter physics with magnetometry based on nitrogen-vacancy centres in diamond. Nature Reviews Materials **2018**, 3, 1–13.
- (21) Dréau, A.; Lesik, M.; Rondin, L.; Spinicelli, P.; Arcizet, O.; Roch, J.-F.; Jacques, V. Avoiding power broadening in optically detected magnetic resonance of single NV defects for enhanced dc magnetic field sensitivity. Physical Review B—Condensed Matter and Materials Physics **2011**, 84, 195204.
- (22) Phan, M.-H.; Peng, H.-X. Giant magnetoimpedance materials: Fundamentals and applications. Progress in Materials Science **2008**, 53, 323–420.
- (23) Mohri, K.; Kawashima, K.; Kohzawa, T.; Yoshida, H. Magneto-inductive element. IEEE Transactions on Magnetism **1993**, 29, 1245–1248.
- (24) Kawashima, K.; Kohzawa, T.; Yoshida, H.; Mohri, K. Magneto-inductive effect in tension-annealed amorphous wires and MI sensors. IEEE Transactions on Magnetism **1993**, 29, 3168–3170.
- (25) Panina, L. V.; Mohri, K. Magneto-impedance effect in amorphous wires. Appl. Phys. Lett. **1994**, 65, 1189–1191.
- (26) Peng, H.-X.; Qin, F.; Phan, M.-H. Ferromagnetic Microwire Composites: From Sensors to Microwave Applications, 1st ed.; Springer International Publishing, 2016.
- (27) Knobel, M.; Pirota, K. R. Giant magnetoimpedance: Concepts and recent progress. J. Magn. Mater. **2002**, 242-245, 33–40.
- (28) Uchiyama, T.; Mohri, K.; Honkura, Y.; Panina, L. V. Recent advances of pico-Tesla resolution magneto-impedance sensor based on amorphous wire CMOS IC MI sensor. IEEE Trans. Magn. **2012**, 48, 3833–3839.

- (29) Mohri, K.; Uchiyama, T.; Panina, L. V.; Yamamoto, M.; Bushida, K. Recent advances of amorphous wire CMOS IC magneto-impedance sensors: Innovative high-performance micro-magnetic sensor chip. J. Sensors **2015**, 2015.
- (30) Chen, J.; Li, J.; Li, Y.; Chen, Y.; Xu, L. Design and Fabrication of a Miniaturized GMI Magnetic Sensor Based on Amorphous Wire by MEMS Technology. Sensors (Basel) **2018**, 18, 732.
- (31) Yu, G.; Bu, X.; Yang, B.; Li, Y.; Xiang, C. Differential-Type GMI Magnetic Sensor Based on Longitudinal Excitation. IEEE Sensors Journal **2011**, 11, 2273–2278.
- (32) Rondin, L.; Tetienne, J. P.; Hingant, T.; Roch, J. F.; Maletinsky, P.; Jacques, V. Magnetometry with nitrogen-vacancy defects in diamond. Reports Prog. Phys. **2014**, 77.
- (33) Maletinsky, P.; Hong, S.; Grinolds, M. S.; Hausmann, B.; Lukin, M. D.; Walsworth, R. L.; Loncar, M.; Yacoby, A. A robust scanning diamond sensor for nanoscale imaging with single nitrogen-vacancy centres. Nature Nanotechnology **2012**, 7, 320 EP –.
- (34) Kavatamane, V. K.; Duan, D.; Arumugam, S. R.; Raatz, N.; Pezzagna, S.; Meijer, J.; Balasubramanian, G. Probing phase transitions in a soft matter system using a single spin quantum sensor. New Journal of Physics **2019**, 21, 103036.
- (35) Eggers, T.; Thiabgoh, O.; Jiang, S.; Shen, H.; Liu, J.; Sun, J.; Srikanth, H.; Phan, M. Tailoring circular magnetic domain structure and high frequency magneto-impedance of melt-extracted Co<sub>69</sub>.<sub>25</sub>Fe<sub>4</sub>.<sub>25</sub>Si<sub>13</sub>B<sub>13</sub>. 5 microwires through Nb doping. AIP Advances **2017**, 7.
- (36) Gruber, A.; Dräbenstedt, A.; Tietz, C.; Fleury, L.; Wrachtrup, J.; Borczykowski, C. v. Scanning Confocal Optical Microscopy and Magnetic Resonance on Single Defect Centers. Science **1997**, 276, 2012–2014.
- (37) Malatek, M.; Dufay, B.; Saez, S.; Dolabdjian, C. Improvement of the off-diagonal magnetoimpedance sensor white noise. Sensors and Actuators A: Physical **2013**, 204, 20–24.

- (38) Mamin, H.; Sherwood, M.; Kim, M.; Rettner, C. T.; Ohno, K.; Awschalom, D. D.; Rugar, D. Multipulse double-quantum magnetometry with near-surface nitrogen-vacancy centers. Physical review letters **2014**, 113, 030803.
- (39) Momenzadeh, S. A.; Stohr, R. J.; De Oliveira, F. F.; Brunner, A.; Denisenko, A.; Yang, S.; Reinhard, F.; Wrachtrup, J. Nanoengineered diamond waveguide as a robust bright platform for nanomagnetometry using shallow nitrogen vacancy centers. Nano letters **2015**, 15, 165–169.
- (40) Li, L.; Chen, E. H.; Zheng, J.; Mouradian, S. L.; Dolde, F.; Schröder, T.; Karaveli, S.; Markham, M. L.; Twitchen, D. J.; Englund, D. Efficient photon collection from a nitrogen vacancy center in a circular bullseye grating. Nano letters **2015**, 15, 1493–1497.
- (41) Shields, B. J.; Unterreithmeier, Q. P.; de Leon, N. P.; Park, H.; Lukin, M. D. Efficient readout of a single spin state in diamond via spin-to-charge conversion. Physical review letters **2015**, 114, 136402.
- (42) Zadeh-Haghighi, H.; Golami, O.; Kavatamane, V. K.; Barclay, P. E.; Simon, C. Master-equation-based model for infrared-based magnetometry with nitrogen-vacancy-centers-in-diamond cavities: A path to subpicotesla sensitivity at submillimeter scales. Physical Review Applied **2024**, 22, 064015.
- (43) Barry, J. F.; Steinecker, M. H.; Alsid, S. T.; Majumder, J.; Pham, L. M.; O’Keeffe, M. F.; Braje, D. A. Sensitive ac and dc magnetometry with nitrogen-vacancy-center ensembles in diamond. Physical Review Applied **2024**, 22, 044069.
- (44) Barry, J. F.; Turner, M. J.; Schloss, J. M.; Glenn, D. R.; Song, Y.; Lukin, M. D.; Park, H.; Walsworth, R. L. Optical magnetic detection of single-neuron action potentials using quantum defects in diamond. Proceedings of the National Academy of Sciences **2016**, 113, 14133–14138.

- (45) Hämäläinen, M.; Hari, R.; Ilmoniemi, R. J.; Knuutila, J.; Lounasmaa, O. V. Magnetoencephalography—theory, instrumentation, and applications to noninvasive studies of the working human brain. Rev. Mod. Phys. **1993**, 65, 413–497.
- (46) Kwong, J. S.; Leithäuser, B.; Park, J.-W.; Yu, C.-M. Diagnostic value of magnetocardiography in coronary artery disease and cardiac arrhythmias: A review of clinical data. International journal of cardiology **2013**, 167, 1835–1842.
- (47) Chiriac, H.; Tibu, M.; Moga, A.-E.; Herea, D. D. Magnetic GMI sensor for detection of biomolecules. Journal of Magnetism and Magnetic Materials **2005**, 293, 671–676.

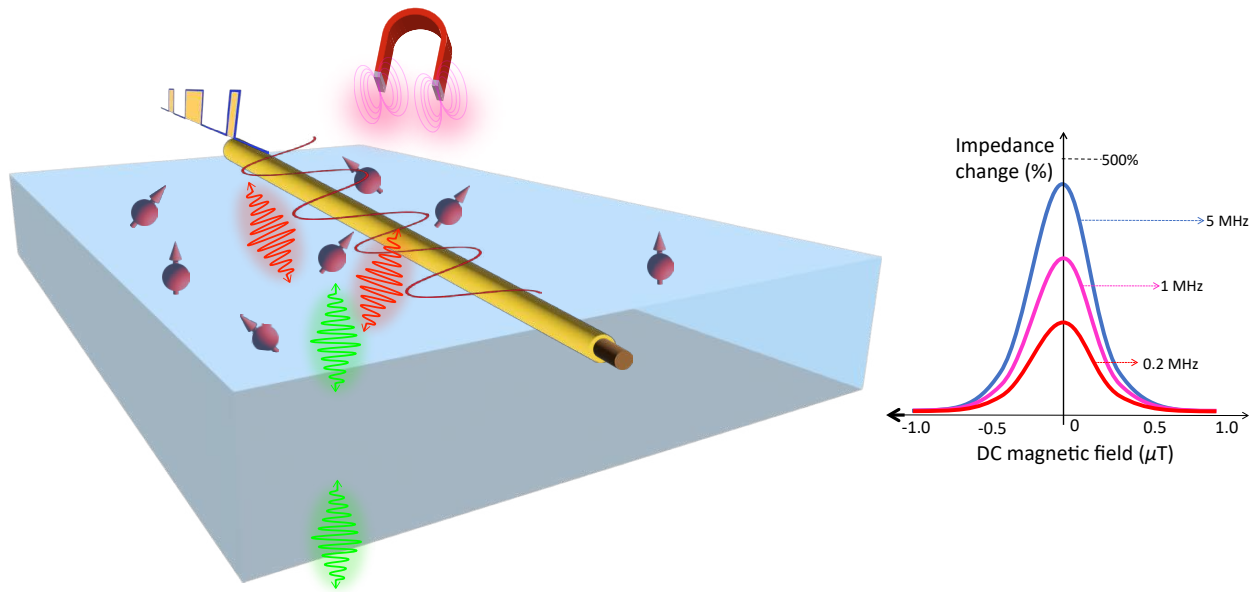


Figure 6: Figure for table of contents

# *Supporting Information for*

# Single-Spin Nitrogen-Vacancy Magnetometer

# with Enhanced Static Field Sensitivity

Vinaya K. Kavatamane,<sup>\*,†,§</sup> Dewen Duan,<sup>†,||</sup> Hadi Zadeh-Haghighi,<sup>‡</sup> Manh-Huong Phan,<sup>¶</sup> and Gopalakrishnan Balasubramanian<sup>\*,†,⊥</sup>

<sup>†</sup>*Max Planck Research Group - Nanoscale Spin Imaging, Max Planck Institute for Biophysical Chemistry, Am Fassberg 11, 37077, Göttingen, Germany*

<sup>‡</sup>*QNeura, Calgary, Alberta T2L 0Y2, Canada*

<sup>¶</sup>*Center for Materials Innovation and Technology, VinUniversity, Hanoi 100000, Vietnam*

<sup>§</sup>*Current address: Institute for Quantum Science and Technology, University of Calgary, Calgary, Alberta T2N 1N4, Canada*

<sup>||</sup>*Current address: School of Physics and Electronic Engineering, Sichuan University of Science and Engineering, Yibin 644005, China*

<sup>⊥</sup>*Current address: XeedQ GmbH, Augustusplatz 1-4, 04109 Leipzig, Germany*

E-mail: vinayakumar.kavatama@ucalgary.ca; gopi@xeedq.com

## **i. Experimental setup**

Experiments were carried out on a home-built confocal microscope using a 532 nm green laser (gem532, Laser Quantum) for NV excitation and an oil-immersion objective (UPlanSApo 60X, NA:1.35) for focusing the laser onto the sample and collecting the NIR fluorescence from it. Following standard confocal method, the fluorescence was focused to a 25  $\mu\text{m}$  pinhole and detected

using two avalanche photo detectors (SPCM-AQRH, EXCELITAS) operating in the Hanbury Brown and Twiss anti-bunching configuration to determine the single NV centers. An acousto-optic modulator, AOM (AA opto-electronic, 200 MHz center frequency) was used in a double-pass scheme to obtain the pulsed laser for the NV spin manipulation. This double-pass AOM pulsing typically achieved a laser extinction ratio (measured by the leaking of laser light when the AOM was turned off) to be  $> 30$  dB. A two channel AWG (model:AWG70002A, Tektronix) operating at a sampling rate of 20 Gsps is the main control unit of our experimental setup. It generates the optical pulses (via AOM), microwave (MW) pulses and the radio frequency driving signals necessary for the experiments. The MW pulses generated in one channel of the AWG are amplified using a 16 W high power amplifier (minicircuits) and applied to the ‘RF port’ of a Bias-Tee Diplexer connector (200B-FF-3, MECA Electronics). The RF driving signal with a maximum amplitude (variable over 0-1 V, peak-to-peak), for driving the GMI wire was generated at the second channel of the AWG and applied to ‘DC or low frequency port’ of the Bias-Tee connector. The output port of the Bias-Tee was then connected to one end of the GMI wire. This way we were able to simultaneously deliver the MW and the RF signal to the GMI wire. The GMI wire was carefully positioned on top of the diamond wafer, with both ends soldered to a home-built microwave stripline circuit designed for  $50 \Omega$  impedance matching. One end of the wire was connected to a 20 W fixed attenuator (Mini-Circuits BW-S20W20+), followed by a  $50 \Omega$  termination (Mini-Circuits ANNE-50+). This setup typically yielded NV center Rabi frequencies of approximately 10 MHz, corresponding to a  $\pi$ -pulse duration of about 50 ns. The test magnetic field ( $B_{dc}$ ) for the magnetometry experiments was produced by passing a known DC current ( $I_{DC}$ ) from a programmable current source (Keithley Model 6221) through a coil positioned near the micro-wire.

## ii. Diamond sample

Shallow NV centers in the high purity (1.1% of  $^{13}\text{C}$  concentration) CVD diamond (from element six) of dimensions  $3 \text{ mm} \times 3 \text{ mm} \times 0.1 \text{ mm}$  were produced by implantation of  $^{15}\text{N}$  ions.<sup>1</sup> For im-

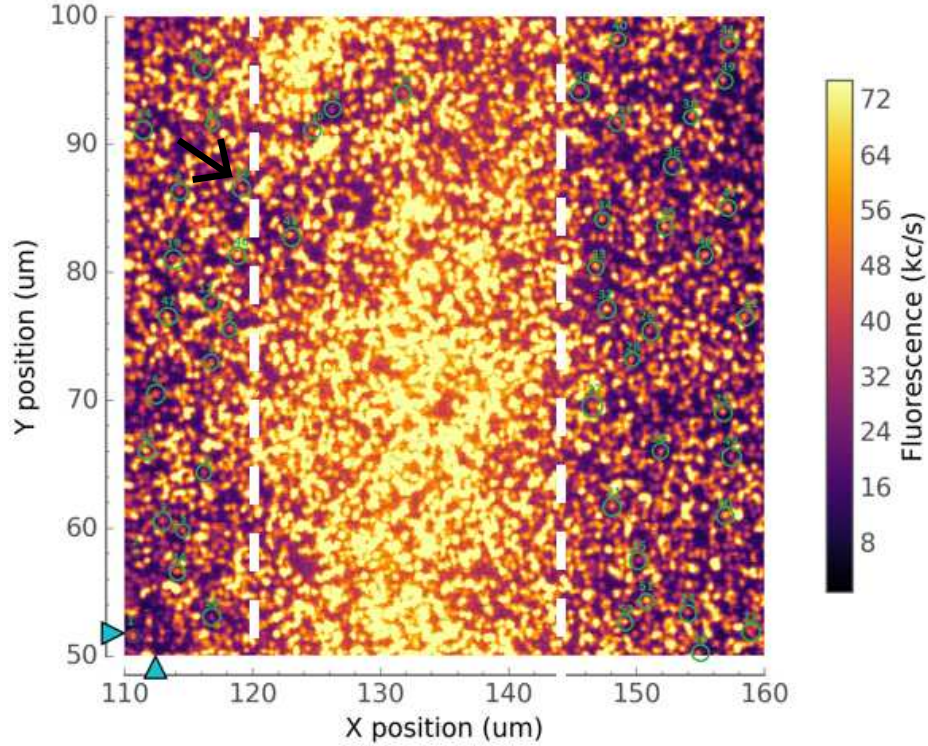


Figure S1: Confocal photoluminescence scan ( $50\ \mu\text{m} \times 50\ \mu\text{m}$ ) of the shallow implanted NVs around the magnetic wire (indicated by white dashed lines). ODMR results from over 70 NV centers were used to reconstruct the magnetic field profile from the wire. Some of the NV centers used for the measurement are shown in green circles. The NV#18 (shown by black arrow near top left corner) was used for the results discussed in the main article.

plantation we used a commercial implanter (SPECS surface Nano Analysis GmbH). We used  $^{15}\text{N}$  ions at a dose of  $10^9$  ions/cm<sup>2</sup> and low energies (2.0 keV) for the shallow implantation. To form NV centers the sample was then subjected to high temperature annealing (800°C) under high vacuum conditions ( $10^{-7}$  mbar) using a commercial vacuum setup (minicoater, tectra GmbH) capable of controllably ramping up/down the temperature. This procedure yielded NV densities good enough to isolate the individual centers under the confocal fluorescence microscope. We expect the NV centers to be at a few nm below the diamond surface based on the standard SRIM simulations.<sup>1</sup> Prior to the experiments, the sample was boiled in a mixture of three acids (sulfuric, nitric, and perchloric acid) at 1:1:1 ratio for several hours. In our case, this acid treatment produces spin dephasing times ( $T_2^*$ ) of single NV centers to be typically around  $1\ \mu\text{s}$  and leaves the surface oxygen terminated.

Figure- S1 shows a confocal image of shallow implanted NV centers in an area of  $50 \mu\text{m} \times 50 \mu\text{m}$  around the GMI wire.

### iii. Giant magneto-impedance (GMI)

Giant magneto-impedance or GMI is a high frequency analogue of well known giant magnetoresistance (GMR), which is the large change in the electrical resistance of a material upon change in the external magnetic field. In both cases (GMI and GMR) one observes a large change in the voltage across the material when the magnetic field is applied. However, GMI and GMR are entirely different concepts in that GMI is purely a classical phenomenon whereas the GMR effect has quantum mechanical origins. The interest in GMI is spurred by several advantages over the conventional magnetic sensors, namely the high sensitivity ( $< \text{nT}$ ) and room temperature operation.

Giant magnetoimpedance is defined as a phenomenon in which under the application of a small alternating current ( $i_{ac}$ ), the AC complex impedance ( $Z$ ) of a soft ferromagnetic conductor undergoes a large change when a tiny static external magnetic field ( $H_{DC}$ ) is applied. This effect is graphically illustrated in Fig.-S2(a) while in Fig.-S2(b) a cylindrical GMI wire under the application of  $i_{ac}$  and  $H_{DC}$  is schematically shown.

The concept of magneto-impedance (MI) has its origin in the well known Skin effect in electromagnetism. The alternating radio frequency (RF) current  $i_{ac} = i_0 e^{j\omega t}$  in a conductive element such as a metal wire, tends to be distributed near the surface (skin) of the conductor (Fig.-S2(c)). This means the current density is not homogeneous over the cross section of the conductor but largest near the surface and decreases exponentially away from the surface. The skin depth ( $\delta_m$ ), the region below the outer surface of the conductor where the effective current flows is given by,

$$\delta_m = \sqrt{2\rho/\omega\mu} \quad (1)$$

where,  $\rho$  is resistivity of the material,  $\omega$ , the angular frequency of the alternating current, and  $\mu_t = \mu_r \mu_0$  (where,  $\mu_r$  and  $\mu_0$  being the relative permeability and permeability of free space,

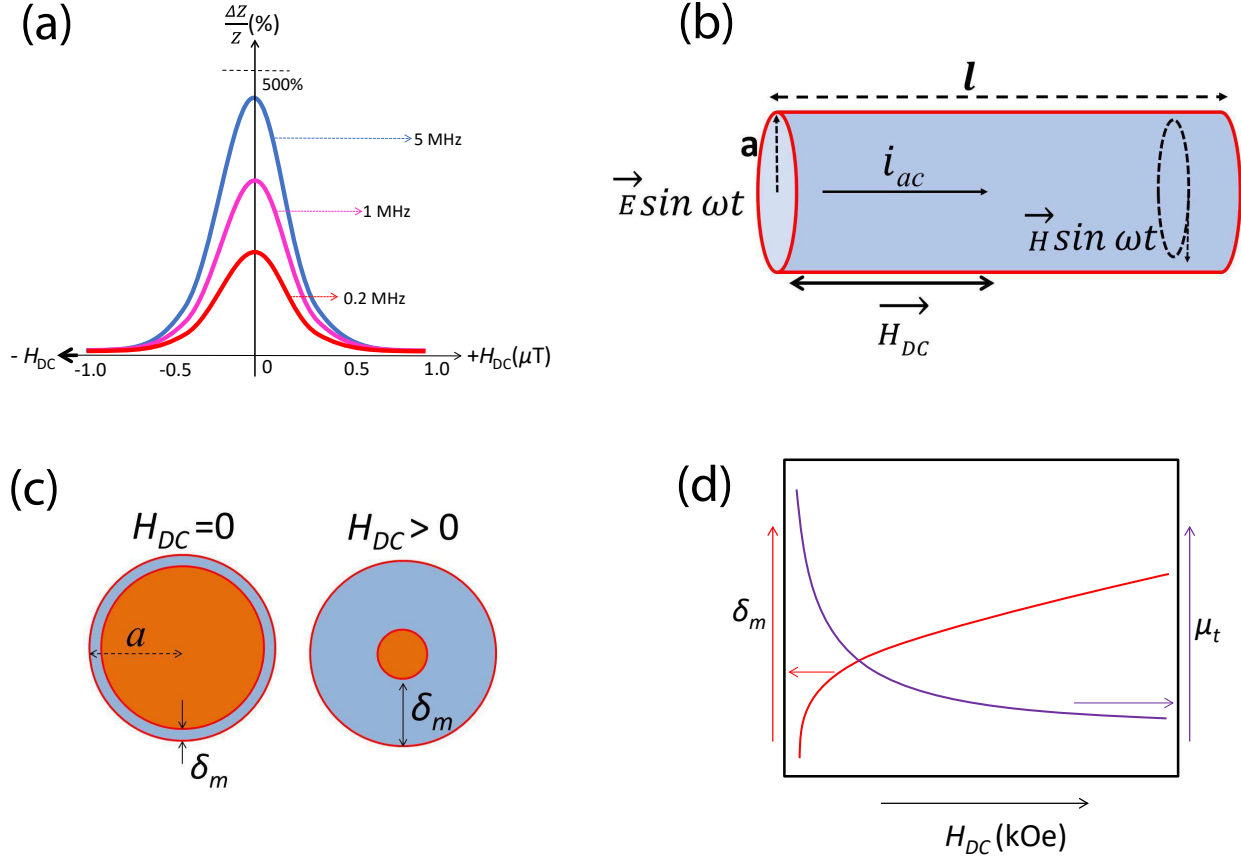


Figure S2: (a) An illustration of a typical frequency and DC magnetic field response of the GMI ratio  $\frac{\Delta Z}{Z}$ . Large change in the  $\frac{\Delta Z}{Z}$  for small changes in the  $H_{DC}$  and its dependence on frequency of radio frequency drive signal can be seen. (b) A schematic illustration of the GMI wire, with length  $l$  carrying the alternating current  $i_{ac}$  and subjected to static external test field,  $H_{DC}$ . (c) An illustration of variation skin depth  $\delta_m$ , with magnitude of  $H_{DC}$ , as seen from the cross section of the GMI wire with a radius of  $a$ . (b) Variation of skin depth (left) and total permeability ( $\mu_t$ ) of the wire as a function of  $H_{DC}$ .

respectively) is the total permeability. From the above equation1 we can expect that as the  $\omega$  increases,  $\delta_m$  decreases which means that the  $i_{ac}$  tends to be concentrated near the surface of the conductor. For ordinary non-ferromagnetic conductors such as copper,  $\mu_t$  is independent of  $\omega$  and the external magnetic field. But for ferromagnetic materials,  $\mu_t$  strongly depends on  $\omega$ , amplitude ( $i_0$ ) of the AC driving current as well as the direction and magnitude of the external applied magnetic field (Fig.-S2(d)). In soft ferromagnetic materials (materials which can be easily magnetized or demagnetized), the permeability  $\mu_t$  changes by orders of magnitude even for the application of small external magnetic fields. The permeability  $\mu_t$  is also sensitive to temperature,

mechanical strain, and magnetic anisotropies in the material.

#### **iv. GMI wire**

For our studies we used a Co-rich amorphous GMI wire with a composition of  $\text{Co}_{69.25}\text{Fe}_{4.25}\text{Si}_{13}\text{B}_{12.5}\text{Nb}_1$  which was fabricated by melt-extraction method.<sup>2</sup> These wires are cylindrical in shape and known to exhibit soft ferromagnetic properties.<sup>3</sup> The wires with a diameter of  $\sim 25 \mu\text{m}$  and length  $\sim 30 \text{mm}$  were used for the experiments. These wires coated with a thin layer (a few microns) of gold using standard electroplating method using a home-built setup involving gold plating solution and a current source (more information is given below). The end to end resistance of the wire was measured to be  $10.2 \Omega$  after the soldering on the stripline. This means for a RF signal with a maximum applied amplitude of 1 V corresponds to an AC current with amplitude of  $\sim 100 \text{mA}$ .

#### **v. Magneto-optical wide field image**

The GMI wire had a diameter of  $\sim 25 \mu\text{m}$ , and due to the inherent magnetic nature of the wire its magnetic field extends to NV centers which are about  $15\text{-}20 \mu\text{m}$  away along the lateral directions (i.e., X and Y-directions the confocal image). Since the wire is magnetic, there exists a spontaneous magnetic field of several Gauss originating from the magnetic domains of the wire at the location of the NV centers. But this field has a spatial profile, in the sense from one point to another along the length of the wire its magnitude and direction change. Figure-S3 is the wide-field magnetic image of the wire reconstructed using an ensemble of over 70 single NV centers in the given area shown in the confocal image in Fig.-S2. The images were created by recording an ODMR spectra for each of the NV in the confocal image. The ODMR spectra gives the information about the absolute value of the static (bias) field ( $\vec{B}$ ) experienced by the NV as well as the orientation of the NV axis ( $\theta$ ) with respect to the bias field direction based on the Zeeman relation  $D_{gs} \pm \gamma_e \cdot |\mathbf{B}_{||}|$  where  $D_{gs}$  is the NV ground state zero field splitting and  $\gamma_e$  is the NV gyromagnetic ratio, and  $\mathbf{B}_{||} = |\vec{B}|\cos\theta$ . The components of the magnetic field along the three orthogonal directions as well

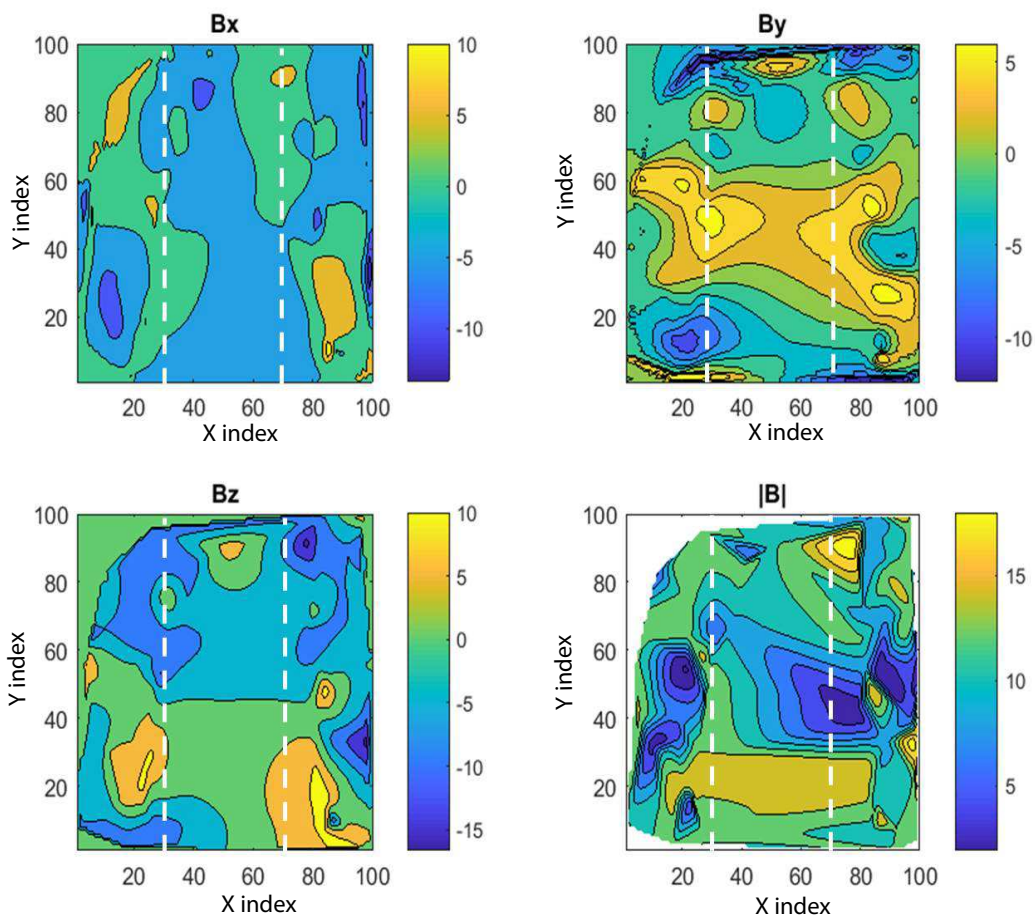


Figure S3: A wide-field magneto-optical image of the GMI microwire generated using NVs in the  $50 \mu\text{m} \times 50 \mu\text{m}$  area.  $B_i$  ( $i = x, y, z$ ) and  $|B|$  are, respectively, the field components along the three orthogonal spatial axes and absolute value of the magnetic field at a given location. Variation of the field values (as indicated by change in color from yellow to blue) can be attributed to the magnetic field from the different magnetic domains in the GMI wire. The numbers on the color bar are in the magnetic field units of Gauss (G). An approximate location of the wire is indicated by the white dashed lines.

as the absolute values of the field are then created as shown in the Fig.-S3.<sup>4</sup> The variation in the field values as indicated by both gradual and abrupt changes in the color signifies the presence of different magnetic domains and domain walls in the amorphous GMI wire, their orientation, and their complex interplay.

Note that no driving alternating current was applied to the wire when these measurements were done.

## vi. Calibrating $B_{dc}$ from the coil

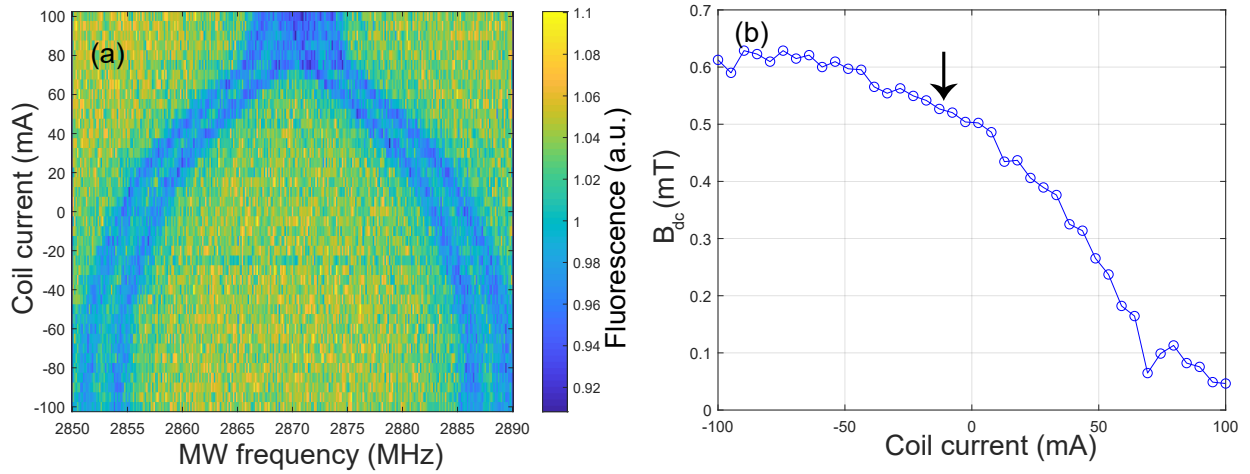


Figure S4: Calibrating the magnetic field generated by current-carrying coil using ODMR. (a) A two-dimensional ODMR spectrum. As mentioned in the Fig.-2(a) of the main article, the two dips in the ODMR spectra correspond to hyperfine interaction of  $^{15}\text{N}$  nucleus with the NV center. The yellow and blue colors in the color bar indicate the  $m_s = \pm 1$  and  $m_s = 0$  sublevels of the NV center, respectively. (b) Extracted values of  $B_{dc}$  at the location of NV center using the detuned frequency in (a). For demonstrating the magnetometry by sweeping the external field in the main article, most linear part of the plot (shown by black arrow) was chosen.

As mentioned before, the test magnetic field ( $B_{dc}$ ) to be detected was applied through a current-carrying coil in the vicinity (a few cm) of the sample. The amount of magnetic field generated from this coil was estimated by using the standard ODMR experiment. Here, the ODMR spectra was recorded for each current values of the sweepable range of the current source. Figure-S4(a) shows such a 2-dimensional scan where the current is swept from -100 mA to +100 mA and the

corresponding NV fluorescence (indicating the  $m_s = 0$  population) across the zero field frequency (2870 MHz) is plotted. The value of  $B_{dc}$  for the corresponding value of current at the location of NV was then extracted using the Zeeman relation mentioned above (Fig.-S4(b)). For calibrating the  $B_{dc}$  for magnetometry experiments, we use only a small section in the most linear portion of the data (black arrow in Fig.-S4(b)) and estimate the amount of  $B_{dc}$  produced over this small current range. We found that the calibration value to be  $2.6 \mu\text{T}/\text{mA}$ . The calibration constant is only valid for this portion since the slope of the curve changes elsewhere.

We note that the ODMR response to the current direction (i.e., current sweeping direction from negative to positive or vice versa) was perfectly reversible with a negligible hysteresis.

The coil was positioned close to the sample and its axis was kept parallel to the GMI wire such that the direction of the DC magnetic field lines emanating from the coil are approximately parallel to the length of the wire. This allows us to take advantage of direction dependent response of the GMI wire to obtain maximum sensitivity for weak external DC fields.

## **vii. Tuning GMI response–optimization of the sensor**

To maximize and stabilize the GMI response to external fields, the GMI wire was subjected to metal electrodeposition and Joule heating or annealing prior to using it for any NV measurements. Since for NV-GMI sensor the GMI wire needs to be electrically contacted (like through soldering) to the coplanar waveguide, poor wettability of the wire results in the increased contact resistance and destabilized Z-response of the wire. In order to overcome this, the GMI wires were deposited with thin layer of gold through the standard process of electroplating.<sup>5</sup> The GMI wire was immersed in a standard gold electroplating solution and a current density of  $\sim 5 \text{ mA}/\text{cm}^2$  was applied for a duration of 10 minutes at room temperature. This produced a few  $\mu\text{m}$  thick layer of gold on the surface of  $\sim 25 \mu\text{m}$  diameter GMI wire. See Fig.-S5(a) for a scanning electron micrograph image of the similar gold plated wire used for the studies reported here. For experimental characterization of the performance of the wire, we employ the similar protocol mentioned in Fig.-3(a)

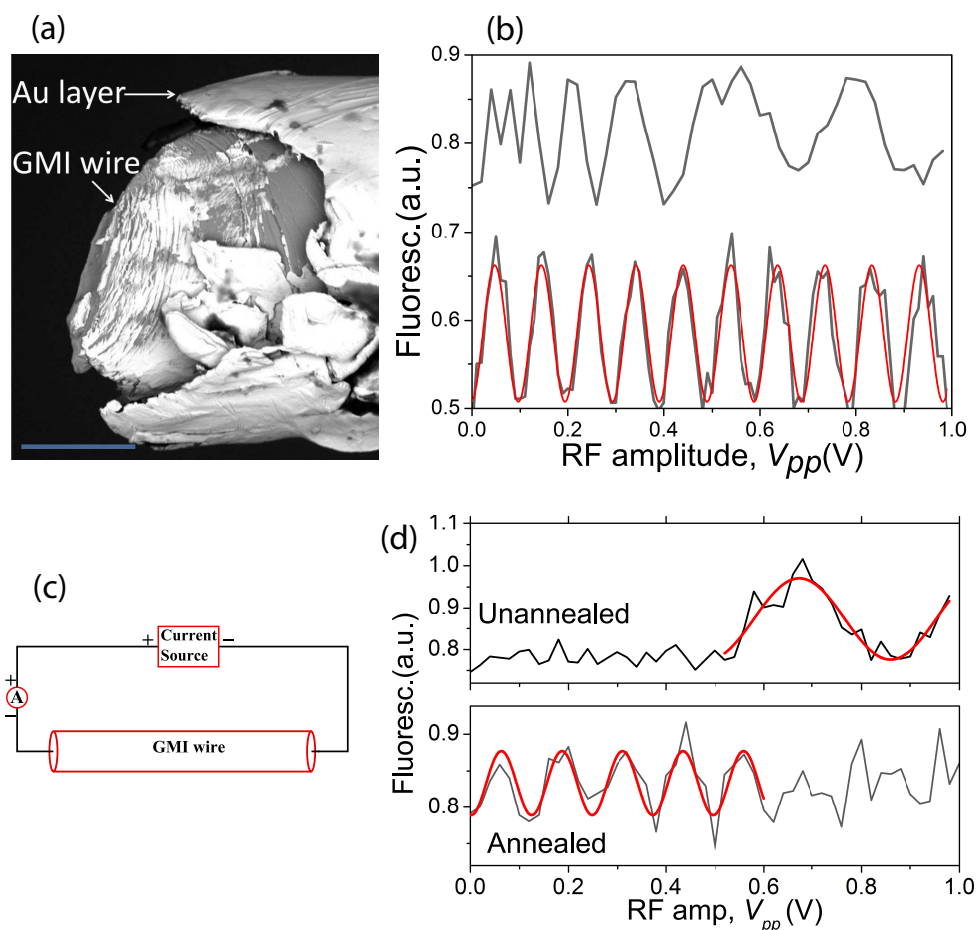


Figure S5: Optimizing GMI wire's material properties. (a) An SEM image of a gold plated GMI wire at its fractured end. Scale bar is  $10\ \mu\text{m}$ . (b) A typical Hahn-echo response for the un plated or pristine (top data) and gold-plated (bottom trace). The echo signals are offset along vertical axis for clarity. Joule-heating the GMI wire, (c) and (d). (c) Joule heating schematic diagram. (d) Effect of Joule heating can be seen by comparing Hahn-echo response of the same wire before and after the process. The data in (b) and (d) were acquired by amplifying the RF signal amplitude with an amplifier gain of 10. The red line in each case is a sinusoidal fit.

of the main text but with following changes: (i) No external field ( $B_{dc}$ ) was present in the coil and (ii) the RF amplitude was not constant but swept from 0 to a known value. In such a measurement scheme, the typical Hahn-echo response of the plated wire in comparison to that of the pristine (unplated) wire is shown in the Fig.-S5(b). Here, the amplitude of the RF signal (as usual applied through the second channel of the AWG) is ramped and the NV Hahn sequence is locked to this RF drive in frequency and the phase. In this particular configuration, the oscillations stem from the NV Hahn response to changes in the AC signal amplitude. Irregular and somewhat non-linear response of the pristine wire are suppressed by the presence of the gold plating which produces smooth and stable oscillations in the magnetometer signal. It is worth noting that even though apparently the unplated wire shows fast oscillations at low voltages ( $< 0.2$  V), this did not translate into any improvements in the DC sensing capability of the hybrid sensor. It should also be noted that the thickness of the plated Au layer has to be carefully adjusted to get optimum sensitivity. For too thin layer of plating (less than about  $1 \mu\text{m}$ ), the magnetometer shows the typical bare-wire characteristics. For too thick Au coating (over  $10 \mu\text{m}$  or so), the GMI properties tend to be suppressed due to the dominance of gold layer and the wire behaves like an ordinary metal antenna.

It has been reported that subjecting GMI materials to high temperatures by passing a direct current—known as Joule-current annealing—can stabilize their magnetic and mechanical properties, thereby enhancing their suitability for sensing applications.<sup>6</sup> This process modifies the GMI response to improve sensitivity to external magnetic fields. Typically, Joule heating is performed using currents close to 100 mA.

In our study, we investigated the Joule heating of a gold-plated wire and observed that this treatment increases sensitivity compared to an unannealed wire, as illustrated in Fig.-S5(c) and (d). Fig.-S5(d) presents an example where the NV Echo signal (at  $B_{dc} = 0$ ) is compared before and after annealing. In the unannealed state, signal oscillations only begin at higher RF drive amplitudes, completing one cycle at the point of maximum peak-to-peak voltage ( $V_{pp}$ ). Joule annealing was performed by passing a high direct current through the wire using a current source,

as shown schematically in Fig.-S5(c). The current was increased incrementally from 0 to 100 mA in 20 mA steps, with each step applied for 10 minutes, followed by a 10-minute pause before the next. The annealed wire exhibited an enhanced NV Echo response, evident from the appearance of oscillations at lower RF drive amplitudes.

However, this enhancement was not consistently observed across all wires studied; in some cases, no significant change was detected after annealing.

### **viii. Sensitivity and noise floor analysis**

For demonstrating the static magnetic field hybrid sensor based on the GMI wire and a single NV center, we employ the basic scheme presented in the Fig.-3(a) of the main text (also replicated in the Fig.-S6(a)). Figure-S6(b) shows the magnetometer response to changes in the external field amplitude. The two datasets represent the same experiment but with the phase of the last (readout)  $\pi/2$  pulse differed by  $180^\circ$ . As explained in the main text, the magnetometer is most sensitive at the highest slope and sensitivity was estimated based on the equation-2 there. The data in Fig.-S6(b) (similar to Fig.-3(b) of the main text) was fitted with a cosine function, and the error value obtained from the fit is divided by the maximum slope of the signal to obtain the minimum detectable field ( $B_{\min}$ ) from which the sensitivity,  $B_{\min}\sqrt{t}$ , was obtained. The measurement time ( $t$ ) used for estimating the sensitivity is given by  $t = \sqrt{2\tau \times n}$ , where  $2\tau$  is the Hahn-echo sequence time ( $= 10 \mu\text{s}$ ) and  $n$  is the number of repetitions used for acquiring the data, which is 500,000 here.

For the noise floor experiment, the Hahn sequence duration was kept constant ( $2\tau = 10 \mu\text{s}$ ) throughout. To determine the noise floor of our hybrid magnetometer, we use the following procedure. We first estimate the magnetometer contrast and divide it by the magnetic field generated by the wire itself to produce that contrast. This is equivalent to determining the slope in the equation-2 of the main text. For estimating the noise floor of the magnetometer, we acquire the magnetometer signal (i.e., recording the photon count trace) over a period of time 1 s at a specific sampling

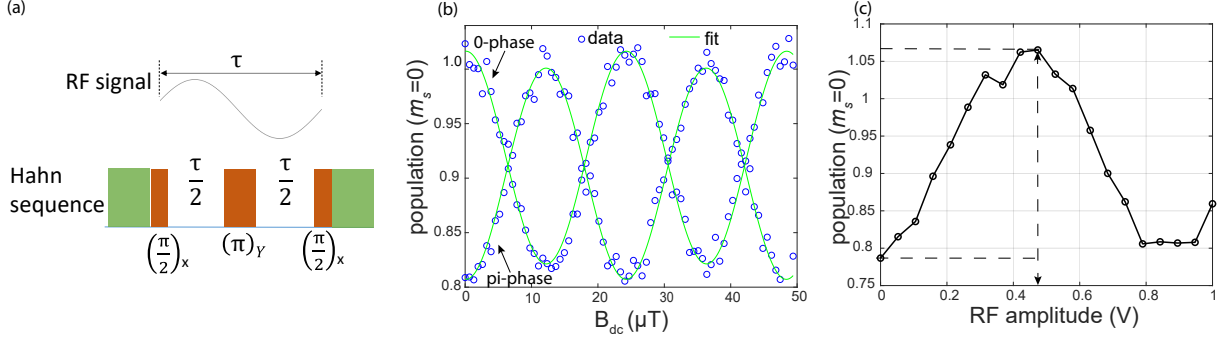


Figure S6: (a) Schematic of the pulse sequence used for sensitivity estimation and noise floor measurement. The sequence is a phase- and frequency-locked Hahn echo protocol referenced to the RF drive signal. (b) A representative magnetometer response showing signal inversion when the phase of the final  $\pi/2$  pulse is shifted by  $180^\circ$ . Here  $2\tau$  was fixed at  $10 \mu\text{s}$ . (c) Measurement of  $\Delta B$  generated due to the GMI wire for estimating the magnetometer's noise floor; data were acquired using the protocol in (a), with the RF drive amplitude varied and no signal amplification applied.

frequency (1 kHz). We then compute the fast Fourier transform (FFT) of this signal. Dividing the FFT amplitude by the slope mentioned earlier gives the minimum detectable field ( $B_{\min}$ ) which is plotted in Fig.5 of the main text.

For estimating the contrast, we use the measurement protocol depicted in Fig.-S6(a) for a fixed Hahn duration of  $10 \mu\text{s}$  and the external test field in the coil being set to 0. We acquire two data sets (not presented here) with the phase of the final  $\pi/2$  pulse of the Hahn sequence set 0 and  $180^\circ$ . We then determine the standard deviations,  $M_1$  (0-phase) and  $M_2$  ( $180^\circ$ -phase), of these two data sets to estimate the magnetometer contrast given by,

$$\Delta M = \frac{M_1 - M_2}{M_1 + M_2} \quad (2)$$

To estimate the magnetic field (note that this field is different from the intrinsic static field emanating from the magnetic nature of the GMI material) generated by the GMI wire due to driving RF current through it, we again employ the protocol depicted in Fig.-S6(a) with a synchronized RF signal while maintaining zero current in the nearby coil. We slowly ramp the amplitude of the RF voltage in steps and record the fluorescence intensity. The variation of NV fluorescence as a function RF amplitude is shown in Fig.-S6(c). It takes about one 0.5 V to invert the NV spin from

its dark to bright state or about 1 V to make one full oscillation in the Hahn signal. Since the Hahn sequence's total duration,  $2\tau$  was set to  $10\ \mu\text{s}$ , we can estimate the magnetic field,  $\Delta B$ , generated over half the oscillation (i.e., in going from dark to bright state) by  $\Delta B = 1/(2\tau\gamma_e)$ , where  $\gamma_e$  is NV gyromagnetic ratio (28 GHz/T). So, the ratio  $\Delta M/\Delta B$  gives the 'slope' of the signal which, along with the FFT amplitude, is then used to estimate the power spectral density showed in Fig.-5 of the main text.

## ix. Intrinsic noise floor of the GMI wire

The intrinsic magnetic noise spectral density,  $\eta_{gmi}$ , that defines the theoretically achievable noise floor for the GMI wire sensors is given by,<sup>7</sup>

$$\eta_{gmi} = \frac{2\alpha k_B T}{\Gamma_e M_s \pi^2 a^2 l}, \quad (3)$$

where,  $\alpha$  is dimensionless damping parameter,  $k_B$  is Boltzmann constant,  $T$  is temperature,  $\Gamma_e$  is the electron gyromagnetic ratio (28 GHz/T),  $M_s$  is the saturation magnetization value. Using the standard values for  $\alpha$  (=0.01) and  $M_s$  (=660 kA/m) as given in the ref<sup>7</sup> for Co-rich GMI wire (like the one used in our case), we approximate the intrinsic noise floor of our wire to be  $\eta_{gmi} \approx 10\text{fT}/\sqrt{\text{Hz}}$  at room temperature. Here, we have used nominal values of  $a$  and  $l$  in our case,  $30\ \mu\text{m}$  and  $10\ \text{mm}$ , respectively. Although the theoretically projected sensitivity is in fT range, however to date, the experimentally reported values for the best noise level are often in the range of  $1\text{pT}/\sqrt{\text{Hz}} - 100\text{pT}/\sqrt{\text{Hz}}$ , at least 2-4 orders of magnitude higher than the theoretical value. Many sources contributing to this limitation have been identified<sup>7,8</sup> with the fundamental limitation being intrinsic magnetic noise associated with the thermal fluctuations of the magnetization of domains in the wire. Other dominant sources include electronic noise in the various circuitry used in the sensor read-out schemes and also from the intrinsic Johnson noise from the GMI wire itself.

## References

- (1) Kavatamane, V. K.; Duan, D.; Arumugam, S. R.; Raatz, N.; Pezzagna, S.; Meijer, J.; Balasubramanian, G. Probing phase transitions in a soft matter system using a single spin quantum sensor. New Journal of Physics **2019**, 21, 103036.
- (2) Wang, H.; Xing, D.; Wang, X.; Sun, J. Fabrication and Characterization of Melt-Extracted Co-Based Amorphous Wires. Metallurgical and Materials Transactions A **2011**, 42, 1103–1108.
- (3) Wang, H.; Qin, F.; Peng, H.; Sun, J. High Performance Soft Magnetic Materials; Springer International Publishing, 2017; Chapter Melt Extracted Microwires, pp 53–89.
- (4) Steinert, S.; Dolde, F.; Neumann, P.; Aird, A.; Naydenov, B.; Balasubramanian, G.; Jelezko, F.; Wrachtrup, J. High sensitivity magnetic imaging using an array of spins in diamond. Review of scientific instruments **2010**, 81.
- (5) Kanani, N. Electroplating: basic principles, processes and practice; Elsevier, 2004.
- (6) Allia, P.; Baricco, M.; Tiberto, P.; Vinai, F. Joule-heating effects in the amorphous Fe 40 Ni 40 B 20 alloy. Physical Review B **1993**, 47, 3118.
- (7) Melo, L.; Ménard, D.; Yelon, A.; Ding, L.; Saez, S.; Dolabdjian, C. Optimization of the magnetic noise and sensitivity of giant magnetoimpedance sensors. Journal of Applied Physics **2008**, 103.
- (8) Ding, L.; Saez, S.; Dolabdjian, C.; Melo, L. G.; Yelon, A.; Menard, D. Equivalent magnetic noise limit of low-cost GMI magnetometer. IEEE Sensors Journal **2009**, 9, 159–168.